Supplement of Weather Clim. Dynam., 6, 1699–1721, 2025
https://doi.org/10.5194/wcd-6-1699-2025-supplement


*Supplement of*

# The role of synoptic circulations in lower-tropospheric dry static energy variability over a South Asian heatwave hotspot

**Hardik M. Shah and Joy M. Monteiro**

*Correspondence to:* Hardik M. Shah (hardik.shah.reach@gmail.com)

## S1 Supplementary figures

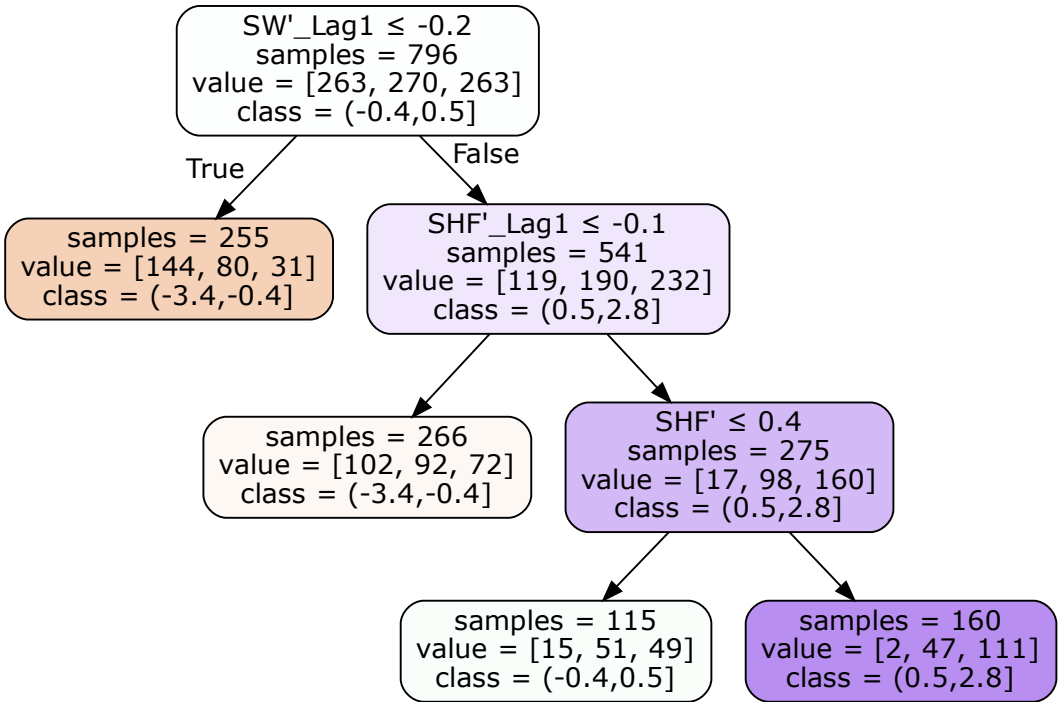


**Figure S1.** Decision tree classification model for tercile based classes of $T'_{2m}$. All the model variables (predictors and outcome) are standardized. The F1-score of the model is 0.6, and the tree growth-stopping criteria were specified as: entropy decrease $\geq 0.03$ at each level, $\geq 30\%$ sample size requirement for level splitting, $\geq 15\%$ sample size requirement for qualifying a leaf node. The variable key for the decision tree model is as follows: SHF$'$: Daily anomalies of sensible heat flux. SW$'$: Daily anomalies of shortwave radiative flux. SHF$'_{Lag1}$: Sensible heat flux anomalies on the previous day. SW$'_{Lag1}$: Shortwave radiative flux anomalies on the previous day. The sign convention for all the above fluxes is positive downwards. It should be noted that positive sensible heat flux anomalies in the above convention usually imply less sensible heat fluxes into the atmosphere.

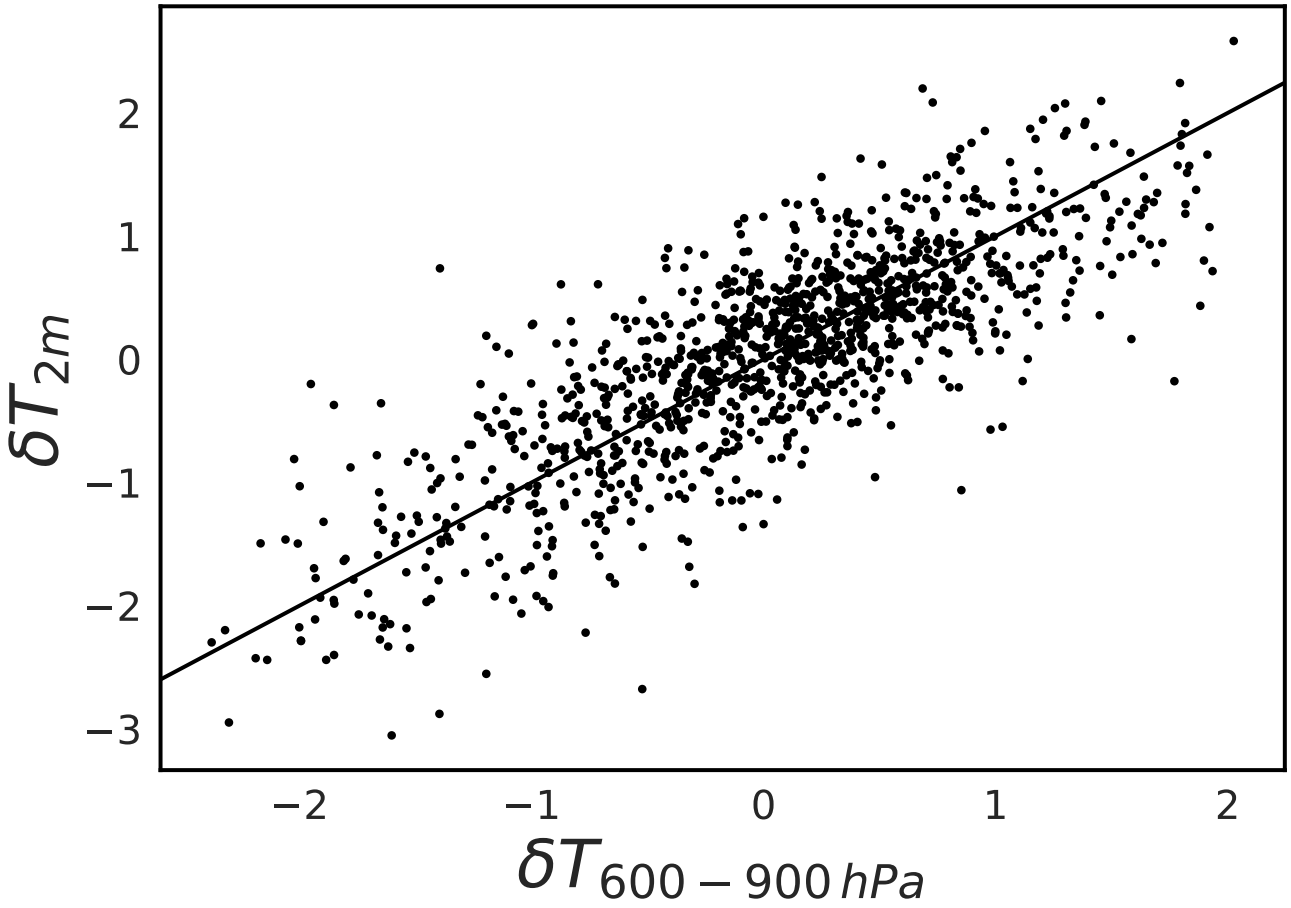


**Figure S2.** Scatterplot of daily lower tropospheric temperature changes ($\delta T_{600-900\,hPa}$) against daily 2m temperature changes $\delta T_{2m}$. The solid line has $\mathrm{slope} = 1$ and passes through the origin.

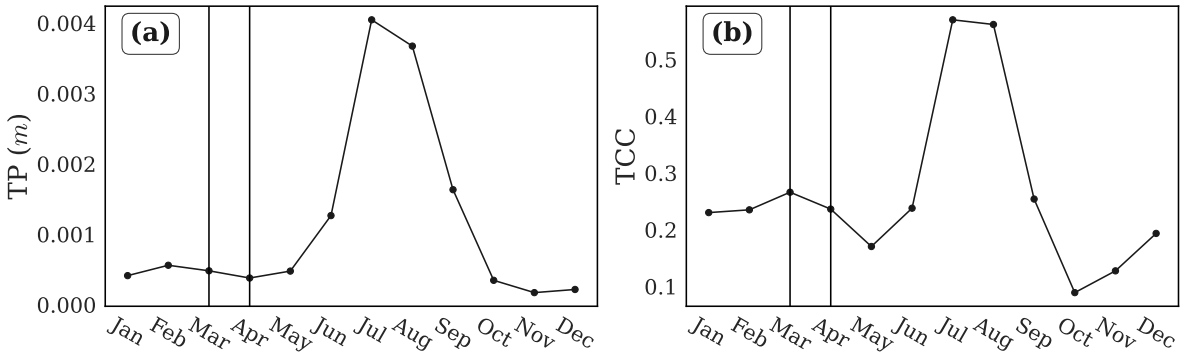


**Figure S3.** Monthly mean quantities computed over the period 1980-2022 using the ERA5 reanalysis product. a) Total Precipitation as the sum of large-scale and convective precipitation, expressed as depth (in $m$) the water would have if it were spread evenly over the region of interest. b) Total cloud cover expressed as the proportion of the entire atmosphere over the region of interest covered by cloud.

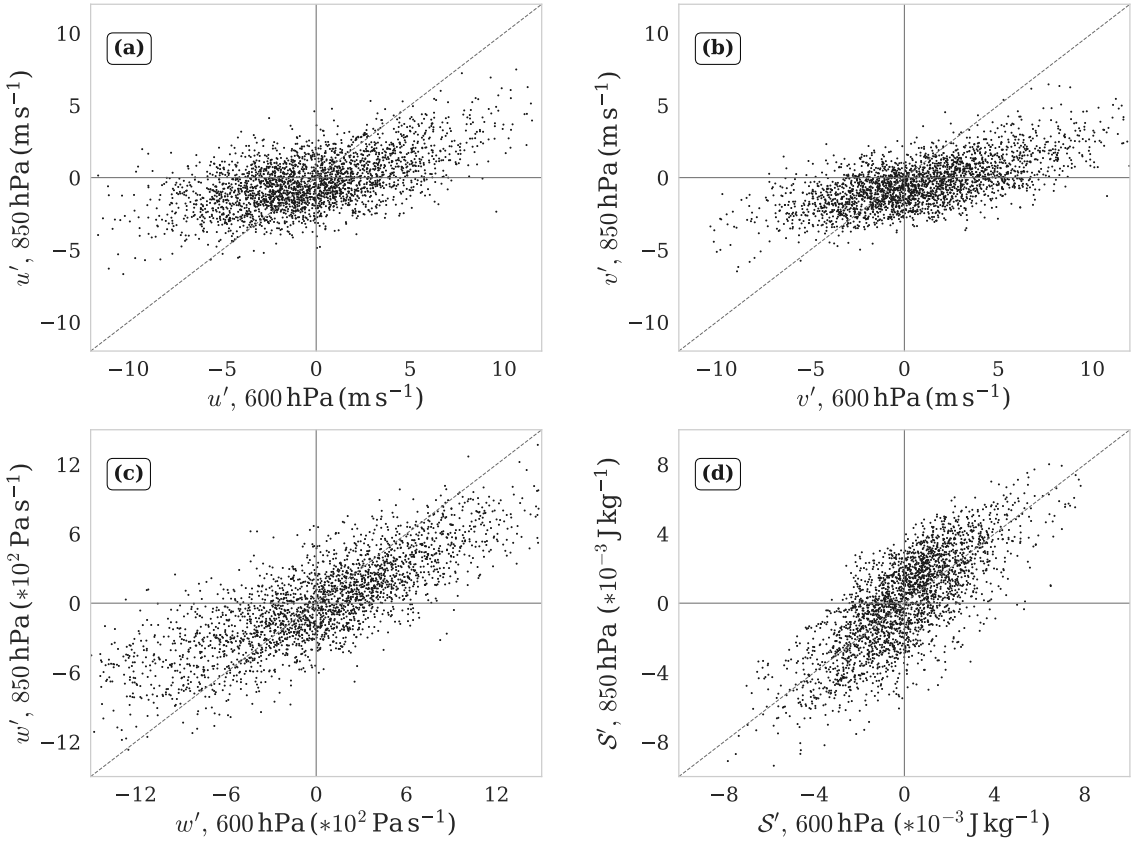


**Figure S4.** For March and April combined, the relationships between 600 hPa and 850 hPa for fields of anomalous wind components and $\mathcal{S}'$. 600 hPa values are plotted on the x-axis, and 850 hPa values on the y-axis. The $x = y$ reference line helps compare the strength of values for these levels. The relationship is positive for all four variables indicating the barotropic nature of these fields. The magnitudes of slopes characterizing the relationships are all $< 1$ except for the $\mathcal{S}'$ plot, indicating that the 600 hPa magnitudes are larger than 850 hPa magnitudes.

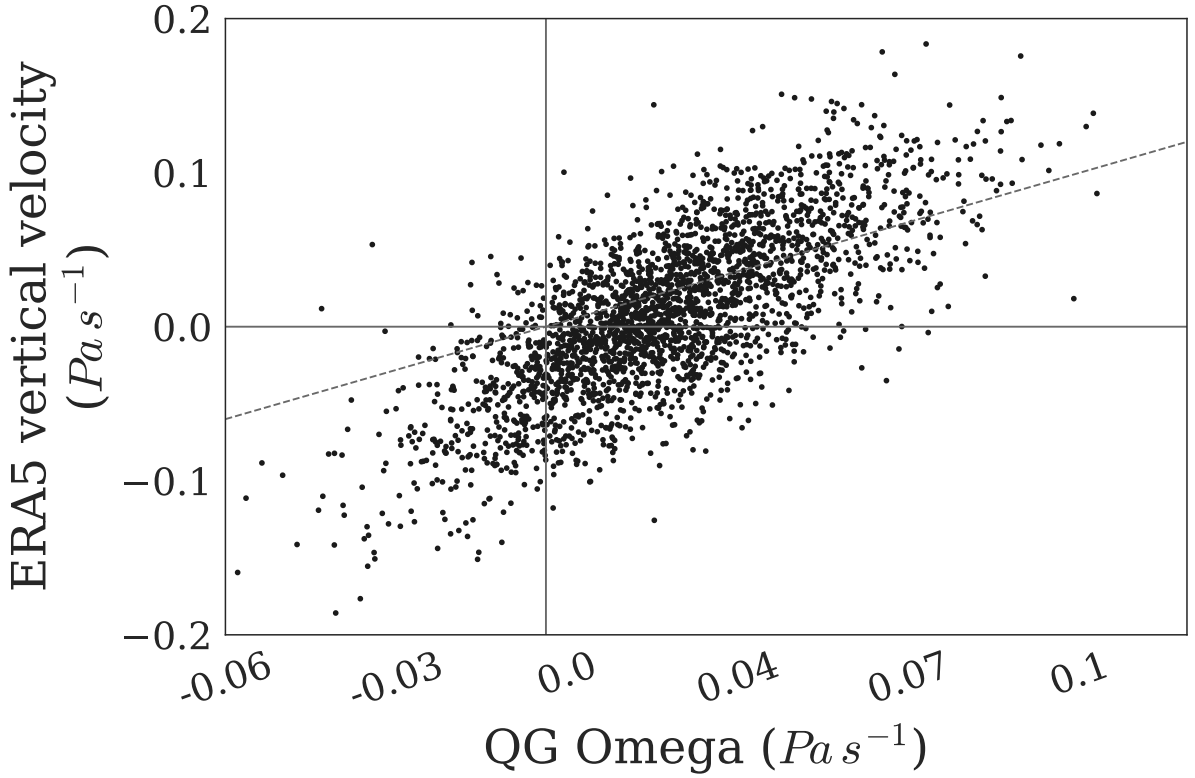


**Figure S5.** The relationship between mass-weighted averages of quasi-geostrophic omega ($\mathrm{Pa s^{-1}}$) and ERA5 vertical velocity ($\mathrm{Pa s^{-1}}$) between 600 hPa to 900 hPa. Quasi-geostrophic omega is numerically solved for by using the *xinvert* Python package Qian (2023) for inverting the omega euqation, $\frac{1}{\partial x}\left(N^2\frac{\partial \omega}{\partial x}\right)+\frac{1}{\partial y}\left(N^2\frac{\partial \omega}{\partial y}\right)+\frac{1}{\partial z}\left(f^2\frac{\partial \omega}{\partial z}\right)=F$ with ERA5 vertical velocity providing the surface boundary conditions. The dashed line is defined by $y=x$.

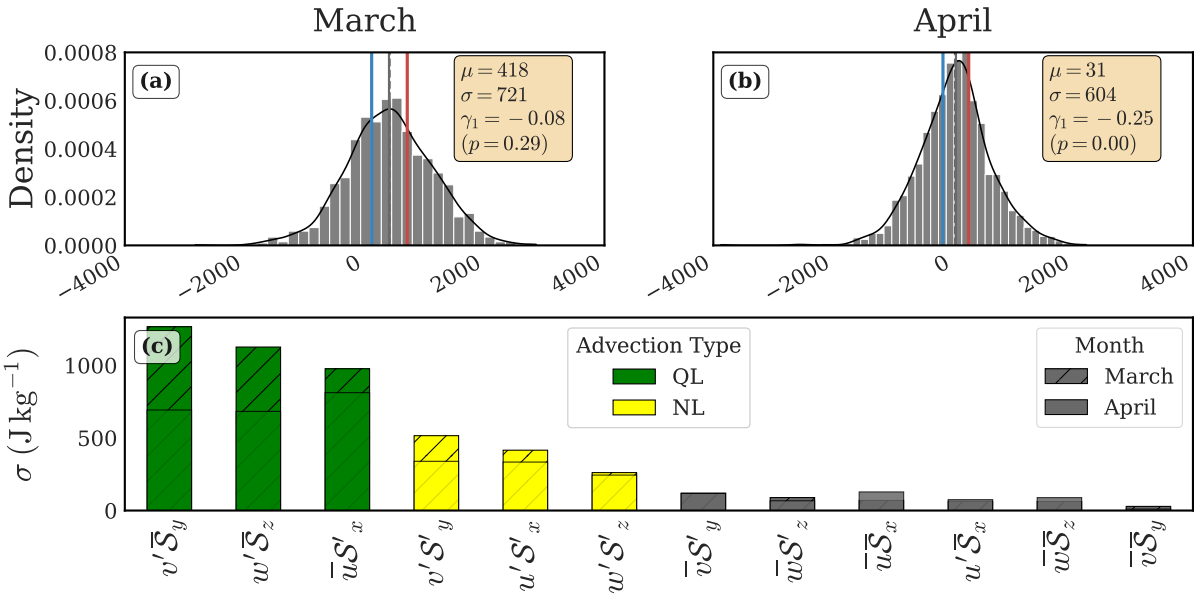


**Figure S6.** The distribution of the 600-900 hPa mass-weighted daily mean advection of DSE, $\delta\mathcal{S}$, for (a) March and (b) April. The blue and red lines demarcate the 33$^{rd}$ and 66$^{th}$ percentiles, respectively. (c) The standard deviation of each of the Reynolds components of advection for both March and April.

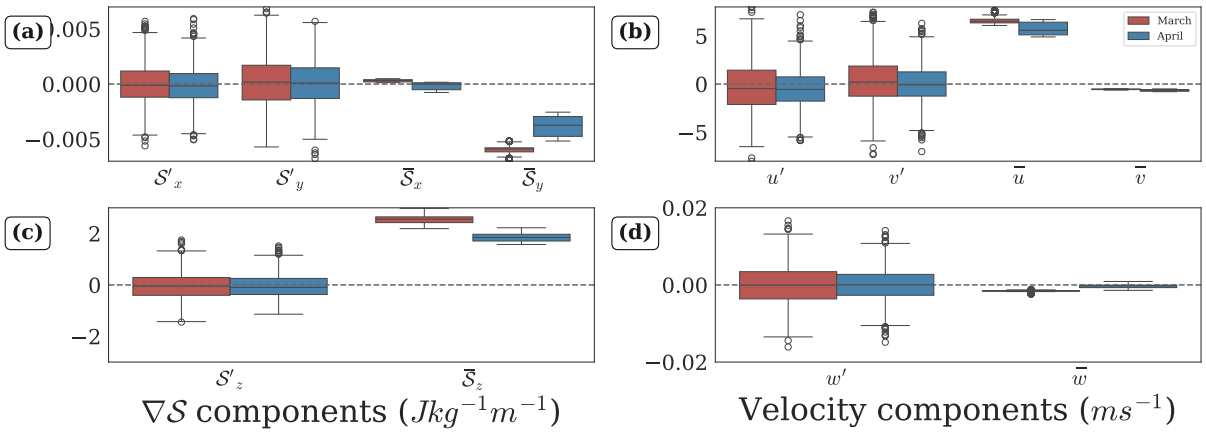


**Figure S7.** For March and April, the distribution of mass-weighted average of fundamental quantities over 600-900 hPa in the region of interest for the March and April periods of analysis: (a) the zonal and meridional derivatives of $DSE$, (b) the zonal and meridional winds, (c) the vertical derivative of $DSE$, (d) vertical winds. *Overbar* represents daily climatology and *prime* represents the related anomalies.

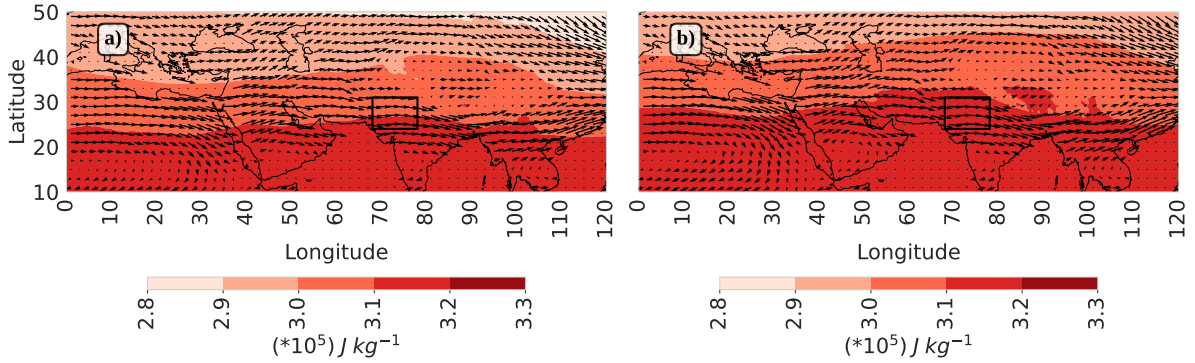


**Figure S8.** Mass-weighted monthly average climatology of horizontal winds (quivers) and DSE (color), between 600-900 hPa over the region for a) Mar, b) Apr. The winds over oceanic regions have been masked because of their large magnitudes as compared to land.

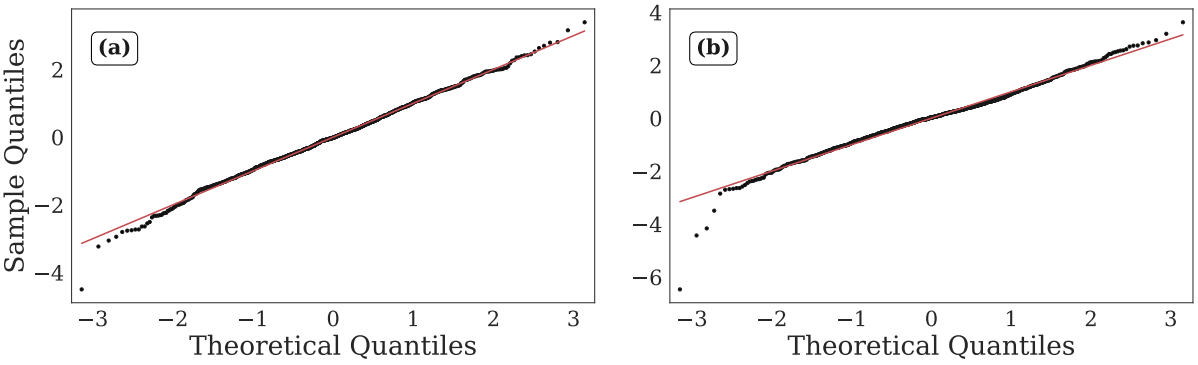


**Figure S9.** Quantile-quantile plots of standardized $\delta\mathcal{S}$ against theoretical standard normal distribution for (a) March and (b) April. Quantiles of the theoretical standard normal distribution were computed from the cumulative distribution function of $\mathbb{N}(0,1)$ using the empirical sample size for each month.

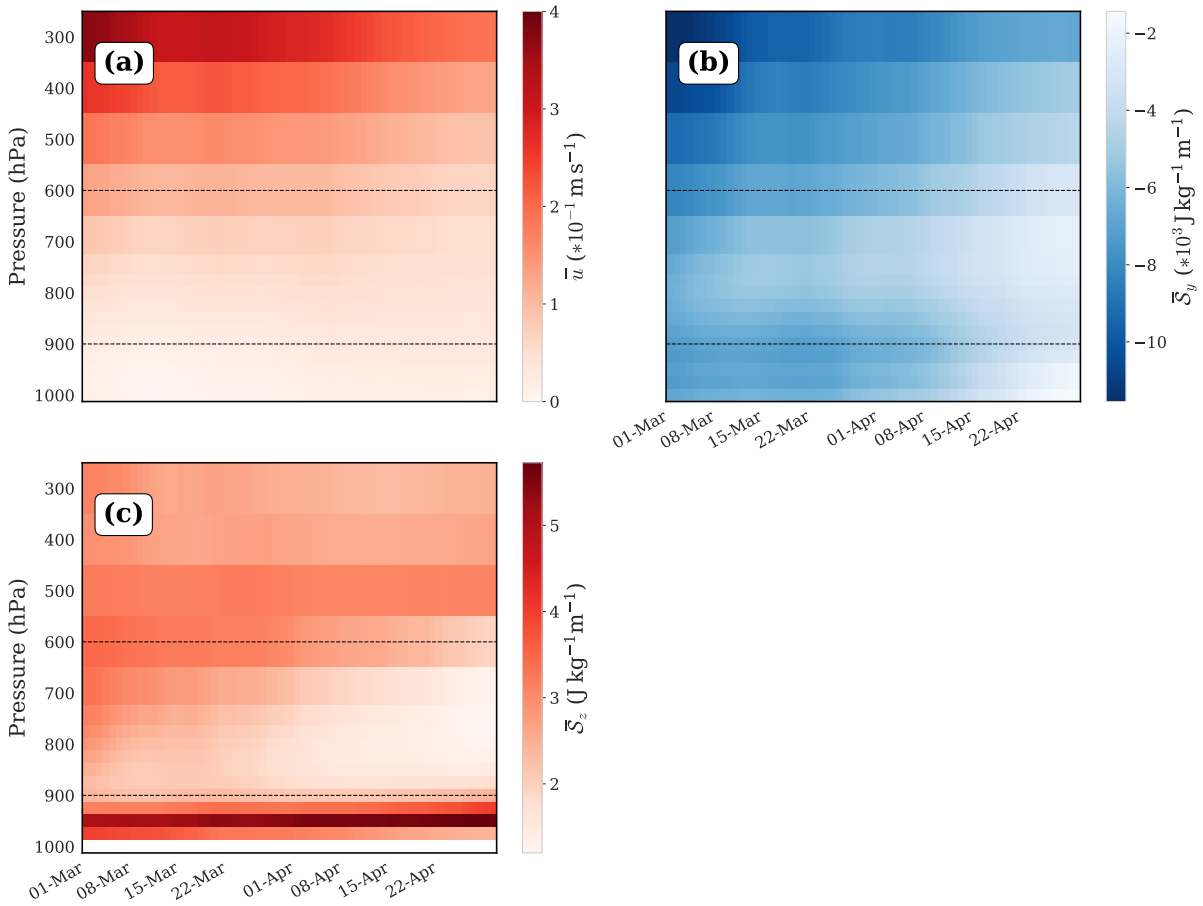


**Figure S10.** The vertical distribution of daily climatology of mass-weighted quantities involved in quasilinear advection. (a) Zonal wind, (b) meridional derivative of $\mathcal{S}$, (c) vertical derivative of $\mathcal{S}$.

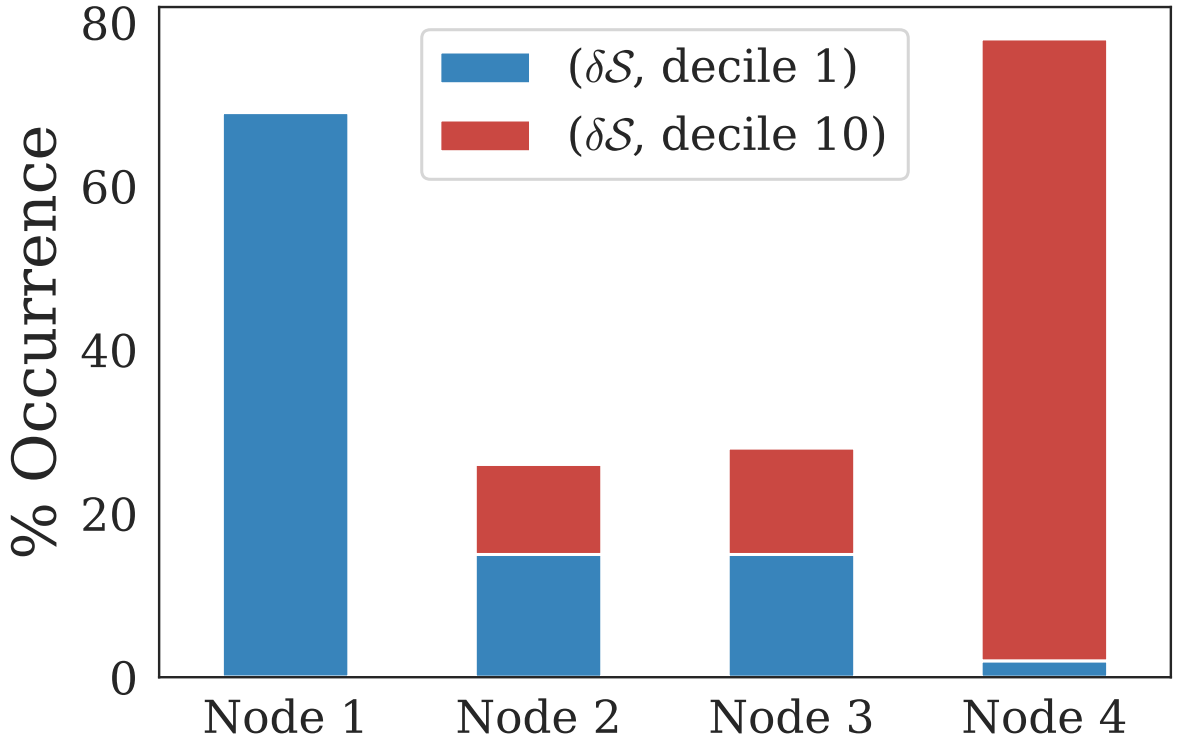


**Figure S11.** During April, the distribution of each of the extreme deciles (1$^{st}$ and 10$^{th}$) of $\delta\mathcal{S}$ across the regions of the primary scatterplot associated with the leaf nodes identified by the primary decision tree.

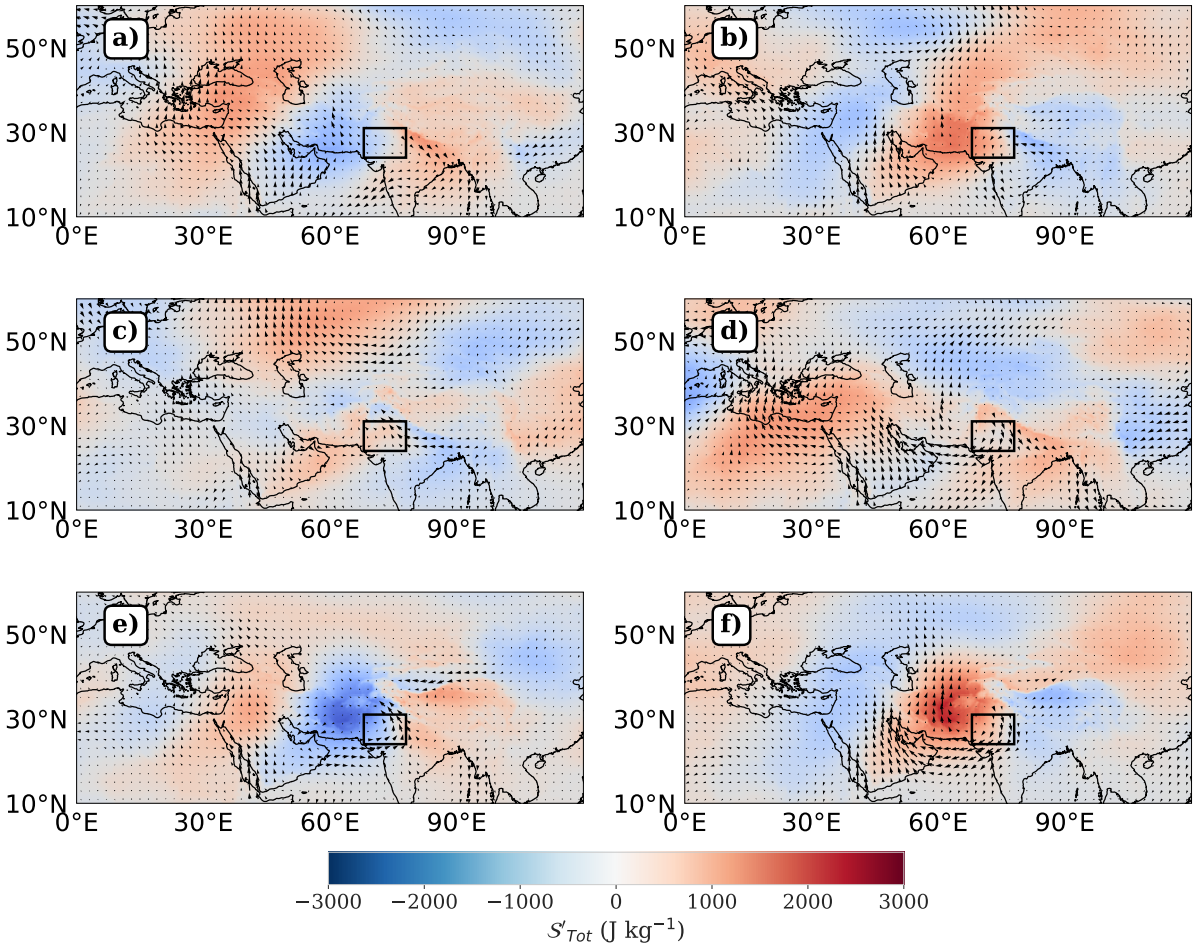


**Figure S12.** April composites of $\mathcal{S}'_{Tot}$ ($J\,kg^{-1}$) anomalies and wind anomalies for different regions in Fig. 2b, corresponding to the following labels. (a) Neutral2, Node 3, (b) Neutral2, Node 5, (c) Neutral1 Node 5, (d) Neutral1 Node 3, (e) Node 2, (f) Node 6.

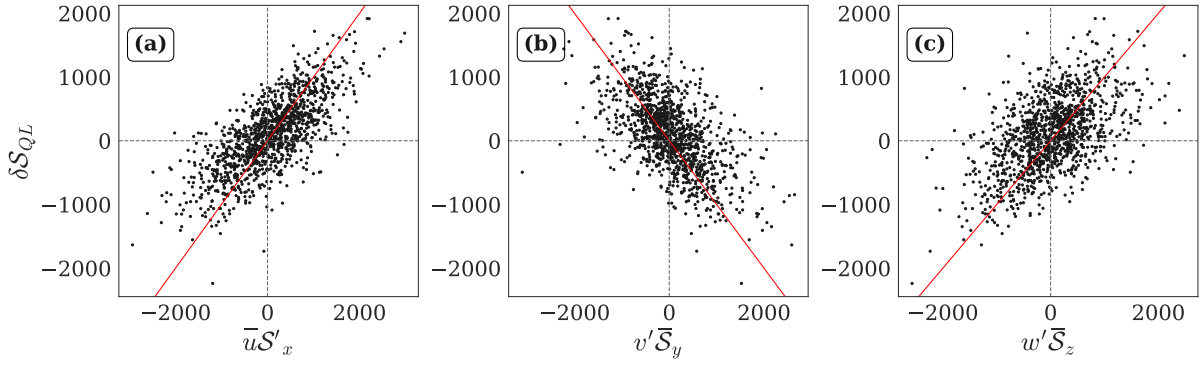


**Figure S13.** During April, the relationship of $\delta\mathcal{S}_{QL}$ with the quasilinear advection components (a) $\bar{u}\mathcal{S}'_x$, (b) $v'\bar{\mathcal{S}}_\dagger$, and (c) $w'\bar{\mathcal{S}}_\ddagger$. All quantities are expressed in $J\,kg^{-1}$. $r_{\delta\mathcal{S}_{QL},\bar{u}\mathcal{S}'_x} = 0.73$, $r_{\delta\mathcal{S}_{QL},v'\bar{\mathcal{S}}_\dagger} = -0.58$, $r_{\delta\mathcal{S}_{QL},w'\bar{\mathcal{S}}_\ddagger} = 0.54$.

| Zonal Terms | Meridional Terms | Vertical Terms |
|---|---|---|
| $\lvert\bar{u}\rvert \sim 10^{1}$<br>$\lvert\bar{\mathcal{S}}_x\rvert \sim 10^{-4}$ | $\lvert\bar{v}\rvert \sim 10^{0}$<br>$\lvert\bar{\mathcal{S}}_y\rvert \sim 10^{-3}$ | $\lvert\bar{w}\rvert \sim 10^{-4}$<br>$\lvert\bar{\mathcal{S}}_z\rvert \sim 10^{0}$ |
| $\frac{\sigma(u')}{\mu(\bar{u})} < 1$<br>$\frac{\sigma(\mathcal{S}'_x)}{\mu(\bar{\mathcal{S}}_x)} >> 1$ | $\frac{\sigma(v')}{\mu(\bar{v})} > 1$<br>$\frac{\sigma(\mathcal{S}'_y)}{\mu(\bar{\mathcal{S}}_y)} < 1$ | $\frac{\sigma(w')}{\mu(\bar{w})} >> 1$<br>$\frac{\sigma(\mathcal{S}'_z)}{\mu(\bar{\mathcal{S}}_z)} < 1$ |

**Table S1.** $\frac{\sigma(a')}{\mu(\bar{a})} : a \in \{u, v, w, \mathcal{S}_x, \mathcal{S}_y, \mathcal{S}_z\}$ is computed for each of the March and April periods, and then averaged over both periods. While most values were consistent across both periods, the ratios involving the zonal gradient and vertical speed were 2x and 5x larger, respectively, during April.

| Coefficient Estimates | | | | | | |
|---|---|---|---|---|---|---|
| **Parameter** | **coef** | **std err** | **t** | **P> \|t\|** | **[0.025** | **0.975]** |
| const | 0.0044 | 0.020 | 0.221 | 0.825 | -0.035 | 0.043 |
| $\delta\mathcal{S}_{\mathrm{QL}}$ | 0.8143 | 0.020 | 40.336 | 0.000 | 0.775 | 0.854 |

| Metric | Value |
|---|---|
| Dep. Variable | $\delta\mathcal{S}$ |
| Model | OLS |
| Method | Least Squares |
| No. Observations | 925 |
| Df Residuals | 923 |
| Df Model | 1 |
| Covariance Type | nonrobust |
| R-squared | 0.638 |
| Adj. R-squared | 0.638 |
| F-statistic | 1627.0 |
| Prob (F-statistic) | $6.94 \times 10^{-206}$ |
| Log-Likelihood | $-844.09$ |
| AIC | 1692.0 |
| BIC | 1702.2 |
| Omnibus | 35.099 |
| Prob(Omnibus) | $2.34 \times 10^{-8}$ |
| Skew | $-0.091$ |
| Kurtosis | 4.527 |
| Durbin-Watson | 1.870 |
| Jarque-Bera (JB) | 91.118 |
| Prob(JB) | $1.64 \times 10^{-20}$ |
| Cond. No. | 1.03 |

**Table S2.** Summary statistics from the OLS regression model predicting $\delta\mathcal{S}$. The model shows strong fit ($R^2 = 0.638$) and highly significant explanatory power (F-statistic p-value $\ll 0.001$).

| Coefficient Estimates | | | | | | |
|---|---|---|---|---|---|---|
| **Parameter** | **coef** | **std err** | **t** | **P> \|t\|** | **[0.025** | **0.975]** |
| const | 0.0023 | 0.008 | 0.290 | 0.772 | -0.013 | 0.018 |
| $\delta\mathcal{S}_{\mathrm{QL}}$ | 0.9630 | 0.008 | 115.738 | 0.000 | 0.947 | 0.979 |
| $\delta\mathcal{S}_{\mathrm{NL}}$ | 0.5777 | 0.008 | 69.289 | 0.000 | 0.561 | 0.594 |

| **Metric** | **Value** |
|---|---|
| Dep. Variable | $\delta\mathcal{S}$ |
| Model | OLS |
| Method | Least Squares |
| No. Observations | 925 |
| Df Residuals | 922 |
| Df Model | 2 |
| Covariance Type | nonrobust |
| R-squared | 0.940 |
| Adj. R-squared | 0.940 |
| F-statistic | 7273.0 |
| Prob (F-statistic) | 0.000 |
| Log-Likelihood | 19.627 |
| AIC | -33.25 |
| BIC | -18.76 |
| Omnibus | 8.889 |
| Prob(Omnibus) | 0.012 |
| Skew | 0.207 |
| Kurtosis | 2.769 |
| Durbin-Watson | 1.928 |
| Jarque-Bera (JB) | 8.665 |
| Prob(JB) | 0.0131 |
| Cond. No. | 1.4 |

**Table S3.** Summary statistics from the OLS regression model predicting $\delta\mathcal{S}$. The model shows strong fit ($R^2 = 0.94$) and highly significant explanatory power (F-statistic p-value $\ll 0.001$).

| Advection Regime | Combo | n_Combo | n_Regime | % Contribution |
|---|---|---|---|---|
| NL Growth | $v'\mathcal{S}'_y \gg 0$ | 10 | 16 | 63% |
| | $u'\mathcal{S}'_x > 0$ | 3 | | 19% |
| | $w'\mathcal{S}'_z > 0$ | 3 | | 18% |
| NL saturated Growth | $u'\mathcal{S}'_x \ll 0$ | 14 | 15 | 93% |
| QL Growth | $u'\mathcal{S}'_x < 0,\ v'\mathcal{S}'_y > 0$ | 20 | 27 | 74% |
| | $u'\mathcal{S}'_x < 0,\ v'\mathcal{S}'_y < 0$ | 5 | | 19% |
| QL Decay | $u'\mathcal{S}'_x < 0,\ v'\mathcal{S}'_y > 0$ | 17 | 32 | 53% |
| | $u'\mathcal{S}'_x < 0,\ v'\mathcal{S}'_y < 0$ | 9 | | 28% |
| | $u'\mathcal{S}'_x > 0,\ v'\mathcal{S}'_y < 0$ | 4 | | 13% |
| | $u'\mathcal{S}'_x > 0,\ v'\mathcal{S}'_y > 0$ | 2 | | 6% |
| NL Decay | $u'\mathcal{S}'_x \ll 0$ | 11 | 21 | 52% |
| | $v'\mathcal{S}'_y \ll 0$ | 10 | | 48% |
| NL Saturated Decay | $v'\mathcal{S}'_y \gg 0$ | 9 | 13 | 69% |

**Table S4.** The frequency distribution of nonlinear combinations per advection regime identified for a pre-existing positive lower tropospheric $DSE$ anomaly (denoted by $\mathcal{S}'_{Tot,Lag1} > 0$) in Fig. 7 in the main text. Table header descriptions as follows. **Combo** lists the nonlinear combinations composed in a given advection regime, **n_Combo** lists the corresponding sample sizes of the nonlinear combinations, **n_Regime** gives the total number of samples in the advection regime, **% Contribution** gives the % contribution of each Combo towards the corresponding advection regime.

| Advection Regime | Combo | n_Combo | n_Regime | % Contribution |
|---|---|---|---|---|
| QL + NL Growth | $u'\mathcal{S}'_x \ll 0$ | 9 | 15 | 60% |
| | $u'\mathcal{S}'_x < 0,\ v'\mathcal{S}'_y < 0$ | 6 | | 40% |
| NL saturated Growth | $v'\mathcal{S}'_y \gg 0$ | 13 | 27 | 48% |
| | $u'\mathcal{S}'_x \gg 0\,(\mathcal{S}'_y < 0)$ | 3 | | 11% |
| | $w'\mathcal{S}'_z > 0$ | 5 | | 19% |
| | $u'\mathcal{S}'_x \gg 0\,(\mathcal{S}'_y > 0)$ | 6 | | 22% |
| QL Growth | $u'\mathcal{S}'_x < 0,\ v'\mathcal{S}'_y > 0$ | 12 | 28 | 43% |
| | $u'\mathcal{S}'_x > 0,\ v'\mathcal{S}'_y > 0$ | 5 | | 18% |
| | $u'\mathcal{S}'_x > 0,\ v'\mathcal{S}'_y < 0\ (\mathcal{S}'_y < 0)$ | 4 | | 14% |
| | $u'\mathcal{S}'_x < 0,\ v'\mathcal{S}'_y < 0$ | 3 | | 11% |
| | $u'\mathcal{S}'_x > 0,\ v'\mathcal{S}'_y < 0\ (\mathcal{S}'_y > 0)$ | 4 | | 14% |
| QL Decay | $u'\mathcal{S}'_x < 0,\ v'\mathcal{S}'_y < 0\ (\mathcal{S}'_y < 0)$ | 12 | 34 | 35% |
| | $u'\mathcal{S}'_x > 0,\ v'\mathcal{S}'_y < 0\ (\mathcal{S}'_y < 0)$ | 7 | | 21% |
| | $u'\mathcal{S}'_x < 0,\ v'\mathcal{S}'_y > 0\ (\mathcal{S}'_y < 0)$ | 1 | | 3% |
| | $u'\mathcal{S}'_x > 0,\ v'\mathcal{S}'_y > 0\ (\mathcal{S}'_y < 0)$ | 1 | | 3% |
| | $u'\mathcal{S}'_x < 0,\ v'\mathcal{S}'_y > 0\ (\mathcal{S}'_y > 0)$ | 11 | | 32% |
| | $u'\mathcal{S}'_x < 0,\ v'\mathcal{S}'_y < 0\ (\mathcal{S}'_y > 0)$ | 2 | | 6% |
| NL saturated Decay | $u'\mathcal{S}'_x \ll 0;\ \mathcal{S}'_y > 0$ | 13 | 21 | 62% |
| | $u'\mathcal{S}'_x \ll 0;\ \mathcal{S}'_y < 0$ | 2 | | 10% |
| | $v'\mathcal{S}'_y \ll 0$ | 3 | | 14% |
| | $u'\mathcal{S}'_x < 0,\ v'\mathcal{S}'_y < 0$ | 3 | | 14% |
| QL + NL Decay | $v'\mathcal{S}'_y > 0,\ w's' > 0$ | 7 | 7 | 100% |

**Table S5.** The frequency distribution of nonlinear combinations per advection regime identified for a pre-existing negative lower tropospheric $DSE$ anomaly (denoted by $\mathcal{S}'_{Tot,\,Lag1} < 0$) in Fig. 9 in the main text. Table headers are described in Table S4.

## S2 Scale analysis of advection terms

$\delta\mathcal{S}$ follows a Gaussian distribution in the body but deviates in the left tail, especially during April (Supplementary Fig. S9) when its skew is significantly negative (tested using D'Agostino's Z-test for skewness; D'Agostino et al. (1990), Virtanen et al. (2020)). The mean value of $\delta\mathcal{S}$ is positive during March due to nonzero mean of nonlinear advection, and zero during April (Figs. S6a, S6b). The standard deviation was larger during March. The mean of most Reynolds components is approximately zero; hence, it is sufficient to use standard deviation as a measure of magnitude. Figure S6c suggests two distinct sets of components with considerable magnitude. The first set has a mean magnitude approximately twice that of the second set for each of the two periods, and includes the three quasilinear advection terms, $v'\bar{\mathcal{S}}_y$, $w'\bar{\mathcal{S}}_z$ and $\bar{u}\mathcal{S}'_x$. The second set comprises nonlinear advection terms, $v'\mathcal{S}'_y$, $w'\mathcal{S}'_z$, and $\bar{u}\mathcal{S}'_x$.

In order to put the observed statistics of these advection terms into dynamical context, we first inspect the background conditions using monthly mean climatology of the directional components of velocity and $\nabla\mathcal{S}$. Both periods March and April are associated with zonally homogenous background conditions, implying strong meridional and weak zonal gradients of $\mathcal{S}$, accompanied by strong zonal winds ($\bar{u}$) and an order of magnitude smaller $\bar{v}$ (Supplementary Fig. monthly boxplots). The horizontal conditions are plotted in Fig. S8. However, the magnitude of the $\nabla\mathcal{S}$ is dominated by $\bar{\mathcal{S}}_z$ owing to large synoptic scale static stability, while the vertical climatological winds are four orders of magnitude smaller than $\bar{u}$. During March, the presence of climatological subsidence in the region makes the stability even higher (Fig. S7).

Second, we evaluate how these climatological values compare with the distribution of anomalies. This comparison is aimed to identify the components governing variability of velocity and $\nabla$S in each direction, with a goal to justify the observed magnitudes of advection components. We find that $\bar{u}$, $v'$ and $w'$ are the primary velocity components, and $\mathcal{S}'_x$, $\bar{\mathcal{S}}_y$ and $\bar{\mathcal{S}}_z$ fields largely govern $\nabla$DSE. It is implied that the dot product of these primary components of $\mathbf{v}$ and $\nabla$DSE in each direction would yield the quasilinear terms, $\bar{u}\mathcal{S}'_x$, $v'\bar{\mathcal{S}}_y$ and $w'\bar{\mathcal{S}}_z$. This observation is consistent with our observation that the quasilinear terms have the largest values of standard deviation (Fig. S6). Even though such an analysis does not provide accurate quantitative estimates of the advective components involved because it treats $\mathbf{v}$ and $\nabla\mathcal{S}'$ separately, it does provide a satisfactory idea of the mechanisms at play because of the barotropic nature of both fields (Fig. S4b, Fig. S4d).

March-April was typically (climatologically) associated with strong meridional and weak zonal gradients of $\mathcal{S}$. However, the magnitude of the climatological gradient of $\mathcal{S}$ was dominated by $\bar{\mathcal{S}}_z$ – which was three orders of magnitude larger than the meridional gradient – owing to large synoptic scale static stability in general (Fig. S7a, Fig. S7c). During Mar, the monthly mean climatological static stability was further amplified possibly by a monthly mean climatology of subsiding winds inhibiting mixing in the vertical (Fig. S7c). On the other hand, the zonal winds ($\bar{u}$) were strongest, accompanied by an order of magnitude smaller $\bar{v}$, and four orders of magnitude smaller $\bar{w}$. In order to arrive at the dominant variability components of velocity and $\nabla \cdot \mathcal{S}$ in each direction, we compared the magnitude of anomalies and respective climatologies using the following approach. Leveraging the fact that the mean of all anomalous quantities was $\sim 0$, a nondimensional quantity was designed to reveal the extent to which most values in the distribution of an anomalous component compared with its relatively constant climatological component. It is given by the ratio of the standard deviation of an anomalous quantity and the mean of its climatological counterpart, and implemented for the various quantities of interest in Table S1. It was seen that $\sigma(u')$ was only a third of the absolute mean of $\bar{u}$, and thus, $\bar{u}$ clearly dominated the regions within $\pm\sigma$, while there was the possibility of comparable magnitudes of $u'$ in the tails. $\sigma(v')$ was thrice as large as the absolute mean of $\bar{v}$, implying that both quantities were comparable only near the mean of $v'$, or zero, while the rest of the space was governed by $v'$. $\sigma(w')$ was ten times larger than the absolute mean of $\bar{w}$, which meant that both quantities were comparable only very close to zero; $w'$ was always dominant everywhere else, and the comprehensive governor of $w$. Thus, one may deduce that primarily it was the $\bar{u}$, $v'$ and $w'$ components that largely governed the velocity fields $u$, $v$ and $w$. Evaluating the directional derivatives of $\mathcal{S}$, it was seen that $\bar{\mathcal{S}}_z$ exceeded $\mathcal{S}'_z$ in its body ($< \sigma$), and was potentially comparable in its tails. A very similar statement could be made about components of the $\mathcal{S}_y$. $\mathcal{S}_x$ was clearly governed by $\mathcal{S}'_x$ strongly across its distribution. Thus, $\mathcal{S}'_x$, $\bar{\mathcal{S}}_y$, $\bar{\mathcal{S}}_z$, largely governed the fields $\mathcal{S}_x$, $\mathcal{S}_y$, and $\mathcal{S}_z$. Given the established preferences, the largest advection terms deductible from such an analysis are $\bar{u}\mathcal{S}'_x$, $v'\bar{\mathcal{S}}_y$, $w'\bar{\mathcal{S}}_z$, which justify the magnitudes observed in Fig. S6.

## References


D'Agostino, R. B., Belanger, A. J., and D'Agostino Jr., R. B.: A Suggestion for Using Powerful and Informative Tests of Normality, The American Statistician, 44, 316–321, 1990.

Qian, Y.-K.: xinvert: A Python package for inversion problems in geophysical fluid dynamics, Journal of Open Source Software, 8, 5510, https://doi.org/10.21105/joss.05510, 2023.

Virtanen, P., Gommers, R., Oliphant, T. E., Haberland, M., Reddy, T., Cournapeau, D., Burovski, E., Peterson, P., Weckesser, W., Bright, J., van der Walt, S. J., Brett, M., Wilson, J., Millman, K. J., Mayorov, N., Nelson, A. R. J., Jones, E., Kern, R., Larson, E., Carey, C. J., Polat, İ., Feng, Y., Moore, E. W., VanderPlas, J., Laxalde, D., Perktold, J., Cimrman, R., Henriksen, I., Quintero, E. A., Harris, C. R., Archibald, A. M., Ribeiro, A. H., Pedregosa, F., van Mulbregt, P., and SciPy 1.0 Contributors: SciPy 1.0: Fundamental Algorithms for Scientific Computing in Python, Nature Methods, 17, 261–272, https://doi.org/10.1038/s41592-019-0686-2, 2020.